The 8th European Congress on Computational Methods in Applied Sciences and Engineering
ECCOMAS Congress 2022
5-–9 June 2022, Oslo, Norway

A MIXED FINITE ELEMENT FORMULATION FOR POLYGONAL ELEMENT GEOMETRIES AND NEARLY-INCOMPRESSIBLE FINITE ELASTICITY

BJORN SAUREN[1*], SIMON KLARMANN[1] AND SVEN KLINKEL[1]

[1]Chair of Structural Analysis and Dynamics
RWTH Aachen University
Mies-van-der-Rohe-Str. 1, 52074 Aachen, Germany
*e-mail: sauren@lbb.rwth-aachen.de

Key words: scaled-boundary, mixed formulation, finite elasticity, volumetric locking

Abstract. In this contribution, the displacement-based scaled-boundary finite element method (SBFEM) is extended to a mixed displacement-pressure formulation for the geometrically and materially nonlinear analysis of nearly-incompressible solids. The displacements and pressures are both parameterized by a scaled-boundary approach, for which an interpolation in the scaling direction is used. Here, higher-order interpolation functions may be employed. It is shown that by introducing the pressure as a field variable, volumetric locking is no longer present. The approach is valid for arbitrary scaling center locations, which can be either inside or outside of the element domain. Other than that, the formulation is valid for non-star-convex element geometries. Numerical examples show that the method is capable of alleviating volumetric locking for arbitrary polygonal meshes and is beneficial in comparison to the displacement-based method when it comes to modeling nearly-incompressible materials.

1 INTRODUCTION

The scaled-boundary finite element method (SBFEM) finds its applications in the field of fracture mechanics [1], quadtree and octree refinement techniques [2], and Voronoi meshes [3]. The transformation of the parameter space into a boundary direction and a scaling direction allows for the description of polygonal element geometries. In the semi-analytical SBFEM [4], the finite element must possess a star-convex geometry. The analytical solution, which is only employed in the scaling direction, makes the method inapplicable to geometrically and physically nonlinear problems. To overcome this deficit, it was shown that one can employ special shape functions in the scaling direction [5], segment the nonlinear differential equation into linear parts [6], or approximate the scaling direction numerically [7, 8].

It was shown in [7], that by approximating the scaling direction with lower-order interpolation functions, volumetric locking can be observed for materials reaching the incompressible limit. Its severity is dependent on the location of the scaling center. In case of an accurately chosen scaling center location, it was observed that volumetric locking could be eliminated for quadrilateral element geometries.

In this contribution, we aim to alleviate volumetric locking and its dependency on the scaling center location for scaled-boundary elements with nearly-incompressible hyperelastic material

laws. The approach originates from [9], where linear quadrilateral acoustic fluid finite elements are modeled by this approach. The weak formulation is derived from a two-field functional, which includes the displacement and pressure as independent field variables. Both quantities are approximated by Lagrangian interpolation functions in both directions, which can be chosen independently. By invoking special pressure continuity requirements in the polygonal element, the volumetric part of the material law is enforced weakly on polygonal element level. This allows for a compressible deformation of the polygon's interior nodes but enforces a nearly-incompressible deformation of the polygonal boundary. We show that by substituting the analytical solution in the scaling direction by a numerical approximation, both star-convex and non-star-convex element geometries can be handled and star-convexity of the element domain is thus no longer required. Other than that, arbitrary scaling center locations, which can be either inside or outside of the element domain, can be chosen.

2 WEAK TWO-FIELD PROBLEM

In this work, the weak form of equilibrium is developed by employing an approach presented in [10]. A pure displacement potential is rewritten into a two-field displacement-pressure potential by employing a Legendre transform:

$$\Pi\left(\mathbf{u},\ p\right) = \int_\Omega W_{dev}\left(\mathbf{C}\right)\ \mathrm{d}V + \int_\Omega p\hat{U}\left(J\right)\ \mathrm{d}V - \frac{1}{2}\int_\Omega \frac{1}{\kappa}p^2\ \mathrm{d}V - \int_\Omega \mathbf{u}^\mathsf{T}\ \mathbf{f}\ \mathrm{d}V - \int_{\partial\Omega} \mathbf{u}^\mathsf{T}\ \bar{\mathbf{t}}\ \mathrm{d}A. \quad (1)$$

Here, the strain energy density function $W\left(\mathbf{C}, J\right)$ has been split into a deviatoric and a volumetric part according to:

$$W\left(\mathbf{C}, J\right) = W_{dev}\left(\mathbf{C}\right) + W_{vol}\left(J\right) = W_{dev}\left(\mathbf{C}\right) + \frac{\kappa}{2}\left[\hat{U}\left(J\right)\right]^2, \quad (2)$$

where κ denotes the material's bulk modulus and $\hat{U}\left(J\right)$ represents the quadratic term of the volumetric strain energy density function. Several possible functions for $\hat{U}\left(J\right)$ exist, however, a suitable choice is to employ a linear function: $\hat{U}\left(J\right) = J - 1$ [11].

The weak formulation is derived from the energy potential in Eq. (1), which is subsequently linearized in the direction of the displacement and pressure increments $\Delta\mathbf{u}$ and Δp as:

$$D_u\left[G_u\left(\delta\mathbf{u}\right)\right]\Delta\mathbf{u} + D_p\left[G_u\left(\delta\mathbf{u}\right)\right]\Delta p = -G_u\left(\delta\mathbf{u}\right) + W_{ext}\left(\delta\mathbf{u}\right), \quad (3a)$$

$$D_u\left[G_p\left(\delta p\right)\right]\Delta\mathbf{u} - D_p\left[G_p\left(\delta p\right)\right]\Delta p = -G_p\left(\delta p\right). \quad (3b)$$

Here, the directional (or Gâteaux) derivatives are defined as:

$$D_u\left[G_u\left(\delta\mathbf{u}\right)\right]\Delta\mathbf{u} = \int_\Omega \delta\mathbf{E} : \mathbb{C} : \Delta\mathbf{E}\ \mathrm{d}V + \int_\Omega \mathbf{S} : \Delta\delta\mathbf{E}\ \mathrm{d}V, \quad (4a)$$

$$D_p\left[G_u\left(\delta\mathbf{u}\right)\right]\Delta p = \int_\Omega \delta\mathbf{E} : \mathbf{S}'_{vol}\ \Delta p\ \mathrm{d}V, \quad (4b)$$

$$D_u\left[G_p\left(\delta p\right)\right]\Delta\mathbf{u} = \int_\Omega \delta p^\mathsf{T}\ \mathbf{S}'_{vol} : \Delta\mathbf{E}\ \mathrm{d}V, \quad (4c)$$

$$D_p\left[G_p\left(\delta p\right)\right]\Delta p = \int_\Omega \delta p^\mathsf{T}\ \frac{1}{\kappa}\ \Delta p\ \mathrm{d}V. \quad (4d)$$

In Eqs. (4a)-(4d), the deviatoric and volumetric second Piola-Kirchhoff stress tensors $\mathbf{S}_{dev}$ and $\mathbf{S}_{vol}$ are defined by the gradients of W_{dev} and W_{vol} with respect to the Green-Lagrange strain tensor $\mathbf{E}$. Furthermore, $\mathbf{S}'_{vol} = \frac{1}{p}\mathbf{S}_{vol}$ holds. The fourth-order tensor $\mathbb{C} = \frac{\partial^2 W}{\partial \mathbf{E} \partial \mathbf{E}}$ is also known as the material tensor.

3 SCALED-BOUNDARY PARAMETERIZATION

The most important characteristic of the scaled-boundary finite element method is the practical description of the polygonal domain. The polygon's edges, which may be discretized into multiple line elements, are parameterized by the boundary parameter $\eta \in [-1,\ 1]$. The scaling direction $\xi \in [0,\ 1]$ describes the polygon's interior and defines the scaling factor applied to the polygonal boundary (see Fig. 1a). The scaling of a single line element towards the so-called scaling center $\mathbf{X}_0$ covers a triangular domain, which is referred to as a section Ω_s (see Fig. 1b). In general, a polygonal domain Ω_e can be subdivided into any number n_s of sections, and thus $\Omega_e = \bigcup^{n_s} \Omega_s$. Consequently, $\partial\Omega_e = \bigcup^{n_s} \partial\Omega_s$ is defined for the polygonal boundary. The aforementioned discretization of the polygonal boundary allows for a numerical approximation in the boundary direction by making use of a set of boundary interpolation functions $\bar{\mathbf{N}}(\eta)$ and the initial nodal coordinates $\tilde{\mathbf{X}}$ of the boundary, resulting in Eq. (5a). The element interior is then defined in Eq. (5b) by simply scaling $\bar{\mathbf{X}}$ towards the scaling center.

$$\bar{\mathbf{X}} = \bar{\mathbf{N}}(\eta)\,\tilde{\mathbf{X}} \qquad \text{on } \partial\Omega_s \tag{5a}$$

$$\mathbf{X} = \mathbf{X}_0 + \xi\left(\bar{\mathbf{X}} - \mathbf{X}_0\right) \qquad \text{in } \Omega_s \tag{5b}$$

To reformulate the kinematical quantities, the deformation gradient $\mathbf{F} = \partial\mathbf{x}/\partial\mathbf{X}$ is rearranged:

$$\hat{\mathbf{F}} = \begin{bmatrix} F_{11} \\ F_{22} \\ F_{12} \\ F_{21} \end{bmatrix} = \begin{bmatrix} \frac{\partial}{\partial X_1} & 0 \\ 0 & \frac{\partial}{\partial X_2} \\ \frac{\partial}{\partial X_2} & 0 \\ 0 & \frac{\partial}{\partial X_1} \end{bmatrix} \begin{bmatrix} x_1 \\ x_2 \end{bmatrix} = \begin{bmatrix} 1 \\ 1 \\ 0 \\ 0 \end{bmatrix} + \begin{bmatrix} \frac{\partial}{\partial X_1} & 0 \\ 0 & \frac{\partial}{\partial X_2} \\ \frac{\partial}{\partial X_2} & 0 \\ 0 & \frac{\partial}{\partial X_1} \end{bmatrix} \begin{bmatrix} u_1 \\ u_2 \end{bmatrix} = \mathbf{i} + \mathbf{D}\mathbf{u}, \tag{6}$$

where $\mathbf{D}$ denotes the differential operator:

$$\mathbf{D} = \underbrace{\begin{bmatrix} \bar{\mathbf{G}}^1 \cdot \mathbf{e}_1 & 0 \\ 0 & \bar{\mathbf{G}}^1 \cdot \mathbf{e}_2 \\ \bar{\mathbf{G}}^1 \cdot \mathbf{e}_2 & 0 \\ 0 & \bar{\mathbf{G}}^1 \cdot \mathbf{e}_1 \end{bmatrix}}_{\mathbf{b}_1} \frac{\partial}{\partial \xi} + \frac{1}{\xi} \underbrace{\begin{bmatrix} \bar{\mathbf{G}}^2 \cdot \mathbf{e}_1 & 0 \\ 0 & \bar{\mathbf{G}}^2 \cdot \mathbf{e}_2 \\ \bar{\mathbf{G}}^2 \cdot \mathbf{e}_2 & 0 \\ 0 & \bar{\mathbf{G}}^2 \cdot \mathbf{e}_1 \end{bmatrix}}_{\mathbf{b}_2} \frac{\partial}{\partial \eta}. \tag{7}$$

The entries in $\mathbf{b}_1$ and $\mathbf{b}_2$ follow from the inverse Jacobian matrix $\bar{\mathbf{J}}^{-1}$ on the boundary, which is constructed from a set of contravariant basis vectors $\bar{\mathbf{G}}^j$ $(j = 1, 2)$ on the boundary:

$$\begin{bmatrix} \frac{\partial}{\partial X_1} \\ \frac{\partial}{\partial X_2} \end{bmatrix} = \underbrace{\begin{bmatrix} \bar{\mathbf{G}}^1 & \bar{\mathbf{G}}^2 \end{bmatrix}}_{\bar{\mathbf{J}}^{-1}} \begin{bmatrix} \frac{\partial}{\partial \xi} \\ \frac{1}{\xi}\frac{\partial}{\partial \eta} \end{bmatrix}. \tag{8}$$

The Green-Lagrange strains in Voigt notation then read:

$$\hat{\mathbf{E}} = \begin{bmatrix} E_{11} \\ E_{22} \\ 2E_{12} \end{bmatrix} = \frac{1}{2} \left(\underbrace{\begin{bmatrix} F_{11} & 0 & 0 & F_{21} \\ 0 & F_{22} & F_{12} & 0 \\ F_{12} & F_{21} & F_{11} & F_{22} \end{bmatrix}}_{\tilde{\mathbf{F}}^{\mathsf{T}}} \underbrace{\begin{bmatrix} F_{11} \\ F_{22} \\ F_{12} \\ F_{21} \end{bmatrix}}_{\hat{\mathbf{F}}} - \begin{bmatrix} 1 \\ 1 \\ 0 \end{bmatrix} \right) . \tag{9}$$

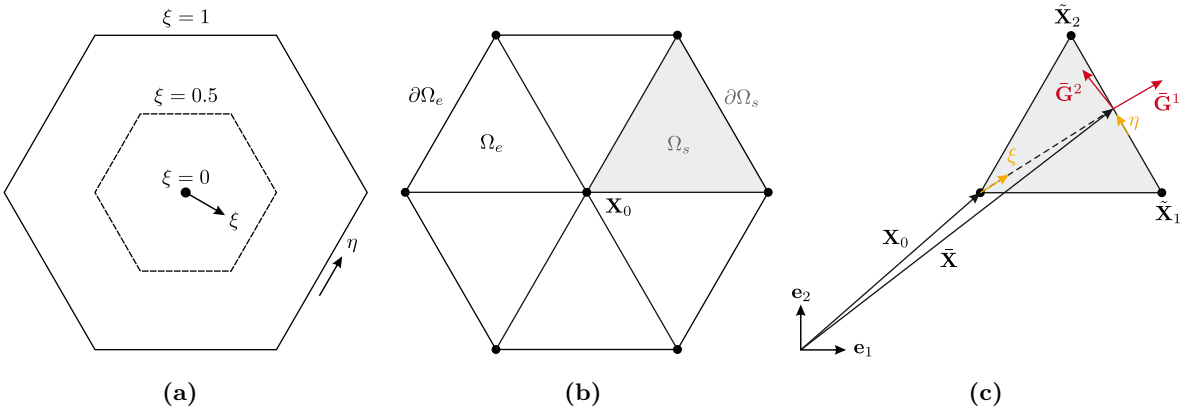

Figure 1: (a) - Definition of the boundary direction η and scaling direction ξ. (b) - Subdivision of a polygonal element into six sections. (c) - Parameterization of a section with contravariant basis vectors on the boundary, spanning the inverse Jacobian.

4 NUMERICAL APPROXIMATION

It was mentioned in Section 2 that the two-field potential consists of two independent field variables, which are the displacement and pressure fields. It is therefore necessary to approximate both field variables by proper interpolation functions according to the scaled-boundary concept. By employing the scaled-boundary parameterization, it is possible to distinguish between four different interpolation orders. Displacement interpolation functions of order p are employed on the element boundary and functions of order q are defined in the scaling direction. The pressure is approximated by interpolation functions of order s on the boundary and order t in the scaling direction. We refer to our mixed scaled-boundary finite elements as B(p, s)S(q, t) elements, where B(p, s) defines the boundary direction and S(q, t) the scaling direction.

Although the Ladyzhenskaya-Babuška-Brezzi (LBB) or inf-sup condition [12] is not proven in this work for the proposed element, we cannot exclude the fact that a violation of the condition might be possible and that numerical instabilities may occur. With this in mind, we choose the interpolation orders for the displacement and pressure in both directions with care (i.e. $p > s$ and $q > t$) and keep in mind that so-called "checkerboard-modes" may occur in our numerical examples. Within the examples presented in this work, however, we have not observed any instabilities which could raise the suspicion that the inf-sup condition is not fulfilled.

The numerical approximation of the displacement field follows the theory presented in [7] and is not further elaborated here. The pressure is approximated by an analogous approach. The pressure on the boundary of a section is constructed by a set of $\bar{n}_p = s+1$ interpolation functions $\bar{N}_i^p(\eta)$ on the boundary, rearranged into a matrix form consistent with Eq. (5a):

$$p^h = \underbrace{\begin{bmatrix}\bar{N}_1^p(\eta) & \bar{N}_2^p(\eta) & \dots & \bar{N}_{\bar{n}_p}^p(\eta)\end{bmatrix}}_{\bar{\mathbf{N}}_p(\eta)} \underbrace{\begin{bmatrix}\tilde{p}_1 \\ \tilde{p}_2 \\ \vdots \\ \tilde{p}_{\bar{n}_p}\end{bmatrix}}_{\tilde{\mathbf{p}}}. \tag{10}$$

Here, $\tilde{p}_i$ indicate all pressures on the sectional boundary $\partial\Omega_s$. The pressures in the scaling direction are approximated by an interpolation matrix $\hat{\mathbf{N}}_p(\xi)$ according to:

$$\tilde{\mathbf{p}} = \underbrace{\begin{bmatrix}\hat{N}_1^p(\xi)\,\mathbf{I}^p & \hat{N}_2^p(\xi)\,\mathbf{I}^p & \dots & \hat{N}_t^p(\xi)\,\mathbf{I}^p & \hat{N}_{\hat{n}_p}^p(\xi)\,\hat{\mathbf{I}}^p\end{bmatrix}}_{\hat{\mathbf{N}}_p(\xi)} \underbrace{\begin{bmatrix}\hat{\mathbf{p}}_t \\ \hat{\mathbf{p}}_{t-1} \\ \vdots \\ \hat{\mathbf{p}}_1 \\ \hat{p}_0\end{bmatrix}}_{\hat{\mathbf{p}}}, \tag{11}$$

where $\hat{N}_i^p(\xi)$ denotes a pressure interpolation function in the scaling direction, $\hat{n}_p = t+1$, $\mathbf{I}^p \in \mathbb{R}^{\bar{n}_p \times \bar{n}_p}$ is an identity matrix and $\hat{\mathbf{I}}^p = \begin{bmatrix}1 & 1 & \dots & 1\end{bmatrix}^\mathsf{T} \in \mathbb{R}^{\bar{n}_p \times 1}$. The pressure belonging to the scaling center is defined as $\hat{p}_0$. The vector $\hat{\mathbf{p}}_j$ with $j = 1, 2, ..., t$ contains the sectional pressures on the line $\xi = \frac{j}{t}$ and reads

$$\hat{\mathbf{p}}_j = \begin{bmatrix}\hat{p}_{j1} & \hat{p}_{j2} & \dots & \hat{p}_{j\bar{n}_p}\end{bmatrix}^\mathsf{T}. \tag{12}$$

Substitution of Eq. (11) into Eq. (10) then leads to the approximated pressure in the sectional domain:

$$p^h = \bar{\mathbf{N}}_p(\eta)\,\hat{\mathbf{N}}_p(\xi)\,\hat{\mathbf{p}} = \mathbf{H}_p(\eta, \xi)\,\hat{\mathbf{p}}. \tag{13}$$

The numerical approximation of a section that belongs to a B(1,0)S(1,0) element is shown in Fig. 2. The approximated nonlinear strain-displacement matrix $\mathbf{B}^h$ [7] and the pressure interpolation matrix $\mathbf{H}_p$ can be inserted into the linearized weak form of Eqs. (3) and lead to a solvable system of equations in the sectional domain Ω_s:

$$\underbrace{\begin{bmatrix}\mathbf{K}_{uu}^s & \mathbf{K}_{up}^s \\ \mathbf{K}_{pu}^s & \mathbf{K}_{pp}^s\end{bmatrix}}_{\mathbf{K}_T^s} \underbrace{\begin{bmatrix}\Delta\mathbf{u}^s \\ \Delta\mathbf{p}^s\end{bmatrix}}_{\Delta\mathbf{v}^s} = \underbrace{\begin{bmatrix}\mathbf{r}_u^s \\ \mathbf{r}_p^s\end{bmatrix}}_{\mathbf{r}^s}. \tag{14}$$

The tangential sectional stiffness matrices $\mathbf{K}_T^s$ are then assembled into their corresponding polygonal stiffness matrices, which are subsequently assembled into the global stiffness matrix. The internal degrees-of-freedom that do not contribute to the continuity between polygonal elements are eliminated by static condensation on polygonal element level.

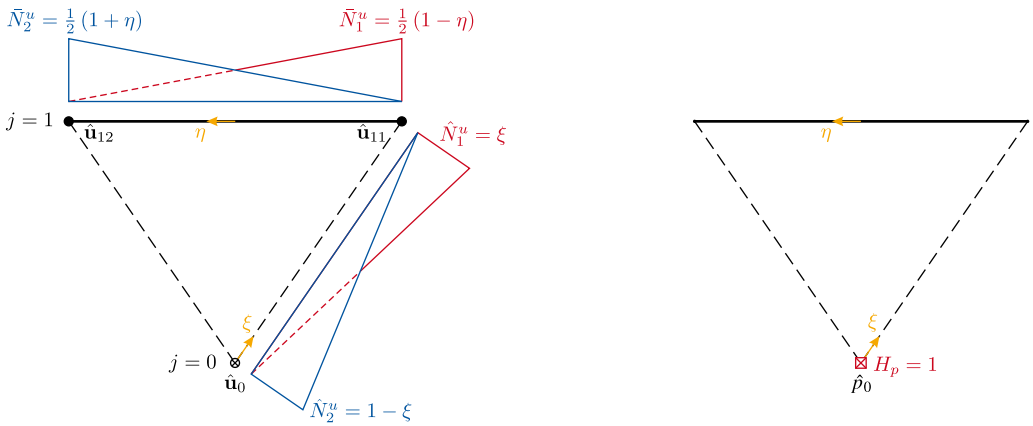

Figure 2: Visualization of a B(1,0)S(1,0) section with corresponding Lagrangian interpolation functions for the displacement (left) and pressure (right).

One should note that the interpolation functions for the pressure are allowed to be discontinuous since the derivation of the pressure does not occur in the weak formulation. To keep mesh generation as simple as possible, the pressure is kept discontinuous over polygonal element boundaries. This allows us to eliminate all pressure degrees-of-freedom on polygonal element level by static condensation. Other than that, the pressure between neighboring sections in the polygonal interior is enforced to be continuous. This is due to the fact that by employing the scaled-boundary parameterization with linear displacement interpolation functions, the strain field in a section remains constant. An independent constant pressure degree-of-freedom in each section would lead to a strong fulfillment of the incompressibility constraint if the pressure is assumed to be discontinuous. The results will then be identical to those obtained by the displacement-based formulation, indicating that the mixed method is still prone to lock volumetrically [13]. By choosing a continuous pressure between sections, the incompressibility constraint is enforced weakly on polygonal element level, which alleviates volumetric locking.

5 NUMERICAL EXAMPLES

In this section, we show that the proposed method does not exhibit volumetric locking as the material's volumetric behavior tends towards the incompressible limit ($\nu \to 0.5$). The examples show that in the proposed formulation, the location of the scaling center does not contribute to volumetric locking. Additionally, it is shown that the numerical approximation and integration of the scaling direction allow for the definition of a scaling center that is located outside of the polygon's kernel area. This feature eliminates the star-convexity criterion which must be fulfilled in the semi-analytical SBFEM [4].

Within the proposed examples, we consider linear displacement and constant pressure interpolation functions with a Neo-Hookean material law, for which the strain energy density function is defined as:

$$\begin{aligned} W(\mathbf{C}, J) &= W_{dev}(\mathbf{C}) + W_{vol}(J) \\ &= \frac{\mu}{2}\left(\operatorname{tr}(\mathbf{C}) - 3\right) + \frac{\kappa}{2}(J-1)^2 . \end{aligned} \tag{15}$$

The elasticity matrix can then be defined in two dimensions by enforcing plane strain conditions.

5.1 Eigenvalue analysis

In this example, it is shown that volumetric locking is alleviated in the proposed formulation and is independent of the scaling center's coordinates. The occurrence of volumetric locking is investigated for both the displacement-based (r1d1) [7] and proposed B(1,0)S(1,0) scaled-boundary elements. The stiffness matrix is constructed for a quadrilateral element with dimensions $b = h = 1$ as depicted in Fig. 3. The material is defined by its Young's modulus $E = 100$ and Poisson's ratio $\nu = 0.4999999999$ under plane strain assumptions. The displacement and pressure degrees-of-freedom which belong to the scaling center are eliminated by static condensation, leaving eight degrees-of-freedom on the polygonal boundary. The eigenvalues λ_i and eigenvectors $\boldsymbol{\phi}_i$ $(i = 1, 2, \dots, 8)$ of the condensed stiffness matrix $\mathbf{K}$ are evaluated according to:

$$(\mathbf{K} - \lambda_i \mathbf{I})\, \boldsymbol{\phi}_i = \mathbf{0}. \tag{16}$$

The occurrence of volumetric locking can be observed from an eigenvalue comparison. Due to the nearly-incompressible material behavior, the eigenvalue λ_8 - which represents the stiffness associated with the volumetric expansion mode of the element (see Fig. 3b) - is expected to tend towards infinity. In an element that is free of volumetric locking, the eigenvalues λ_1 until λ_7 do not interact with the volumetric expansion mode and remain finite for $\nu \to 0.5$.

The eigenvalues and eigenvectors of the stiffness matrix are determined for both element formulations with six different scaling center locations. All scaling center locations $\mathbf{X}_0$ and the corresponding two largest eigenvalues λ_7 and λ_8 are summarized in Table 1. It should be noted that the eigenvector $\boldsymbol{\phi}_7$ is not comparable to the results obtained for a classical quadrilateral (Q1) element [14] and does not represent a pure bending or shear mode.

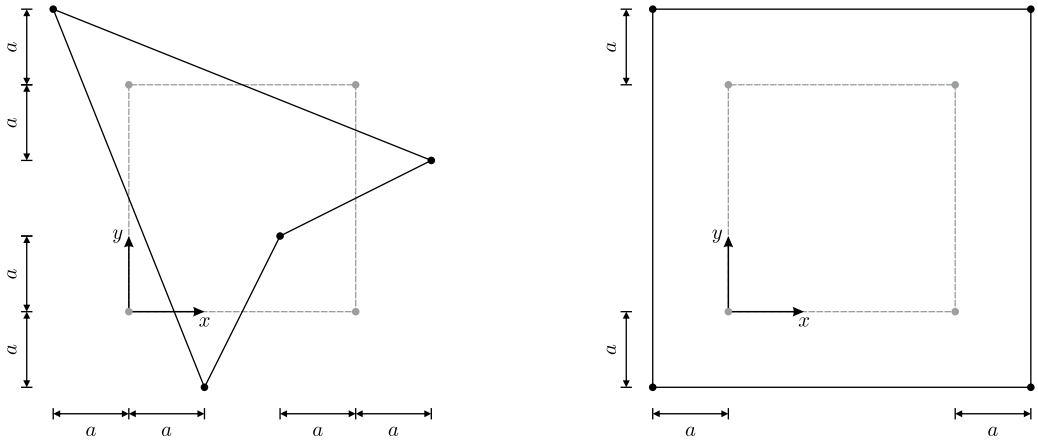

(a) Deformation mode $\boldsymbol{\phi}_7$ **(b)** Volumetric expansion mode $\boldsymbol{\phi}_8$

Figure 3: Eigenvalue analysis. Eigenvectors $\boldsymbol{\phi}_7$ and $\boldsymbol{\phi}_8$ of the stiffness matrix $\mathbf{K}$ for the B(1,0)S(1,0) element with quadrilateral geometry. The displacements and pressure associated with the scaling center are eliminated by static condensation.

It can be recognized from Table 1 that the deformation mode $\boldsymbol{\phi}_7$ and volumetric expansion mode $\boldsymbol{\phi}_8$ are coupled if the quadrilateral is discretized by the displacement-based r1d1 element. An exception is observed if the scaling center is placed at $\mathbf{X}_0 = [0.5 \;\; 0.5]$. It can hence be concluded that the quadrilateral displacement-based scaled-boundary element [7] locks volumetrically if the scaling center does not coincide with the element's barycenter. In fact, this observation follows the conclusion presented in Nagtegaal et al. [15], who stated that the subdivision of a quadrilateral element into four triangular elements meeting at the intersection point of the main diagonals, does not show any volumetric locking.

In the proposed mixed formulation, $\boldsymbol{\phi}_7$ and $\boldsymbol{\phi}_8$ remain uncoupled for any of the chosen scaling center locations listed in Table 1. This indicates that volumetric locking is alleviated in the proposed element formulation and is not associated with the physical coordinates of the scaling center.

Table 1: Eigenvalues λ_7 and λ_8 of the stiffness matrix in dependence of the scaling center location $\mathbf{X}_0$. The eigenvalues marked in red indicate that volumetric locking is present.

$\mathbf{X}_0$		r1d1 [7]		B(1,0)S(1,0)	
x	y	λ_7	λ_8	λ_7	λ_8
0.2	0.2	$\mathbf{1.19 \cdot 10^{11}}$	$3.33 \cdot 10^{11}$	56.38	$3.33 \cdot 10^{11}$
0.9	0.9	$\mathbf{2.13 \cdot 10^{11}}$	$3.33 \cdot 10^{11}$	70.60	$3.33 \cdot 10^{11}$
0.7	0.4	$\mathbf{3.31 \cdot 10^{10}}$	$3.33 \cdot 10^{11}$	41.10	$3.33 \cdot 10^{11}$
0.3	0.95	$\mathbf{1.62 \cdot 10^{11}}$	$3.33 \cdot 10^{11}$	53.10	$3.33 \cdot 10^{11}$
0.1	0.8	$\mathbf{1.66 \cdot 10^{11}}$	$3.33 \cdot 10^{11}$	52.57	$3.33 \cdot 10^{11}$
0.5	0.5	66.66	$3.33 \cdot 10^{11}$	38.05	$3.33 \cdot 10^{11}$

5.2 Non-star-convex patch test

In this example, we demonstrate that the proposed formulation is applicable to arbitrary polygonal element geometries and is able to represent a constant stress state for these elements. A square plate of dimensions $b = 10$ and $h = 10$ is subjected to a uniform tension and shear load $n = 10$, as depicted in Fig. 4a. As in Section 5.1, the material parameters are defined as $E = 100$ and $\nu = 0.4999999999$. The use of plain strain conditions and the constant stress state $\hat{\boldsymbol{\sigma}} = [n \;\; n \;\; n]^\mathsf{T} = [10 \;\; 10 \;\; 10]^\mathsf{T}$ yield a linear analytical solution for the engineering shear strain: $\gamma_{xy} = 2\varepsilon_{xy} = 0.3$.

In the plate's interior, a sub-mesh is constructed consisting of three polygonal elements. Elements 1 and 2 possess a star-convex geometry (there exists a kernel area from which every element node is visible), whereas element 3 is defined by a non-star-convex boundary. The coordinates of the non-star-convex polygon are given in Table 2. The semi-analytical SBFEM would require a partition of element 3 into two star-convex elements (indicated by the blue dotted line in Fig. 4a) in order to obtain the solution to the problem. In the proposed mixed formulation, however, the scaling center can be placed at nearly any arbitrary location, which can be either inside or outside of the element. This is caused by the fact that the boundary direction η is mirrored for several sections, leading to a sign change in the Jacobian determinant.

Table 2: Nodal coordinates of the non-star-convex polygon in the reference configuration.

	①	②	③	④	⑤	⑥
X	5.0	7.0	5.0	5.0	3.0	5.0
Y	1.0	6.0	5.5	9.0	4.0	4.5

The sectional stiffness matrices are then either "added" (positive determinant) or "subtracted" (negative determinant) from the polygonal element's stiffness matrix. Overall, this leads to the exact integration of the stiffness matrix over the polygonal domain [16].

To test the robustness of the scaling center location, the scaling center $\mathbf{X}_0^3$ is placed at several randomly generated locations, both inside and outside of element 3. The analytical solution $\gamma_{xy} = 0.3$ is reached for all tested scaling centers, indicating that the numerical integration of the stiffness matrix is carried out correctly for non-star-convex geometries.

Unfortunately, the numerical approximation of both parametric directions causes a minor deficit. By placing the scaling center at any spatial point which is colinear to any of the element's edges, the Jacobian determinant becomes zero for the corresponding section. This result is physically correct since the area spanned by the colinear edge and the scaling center is equal to zero, but contributes to a numerical problem when inverting the Jacobian matrix. In practice, however, the scaling center can be placed at a random location. The probability that a colinearity between the scaling center and an element edge exists, is then practically equal to zero.

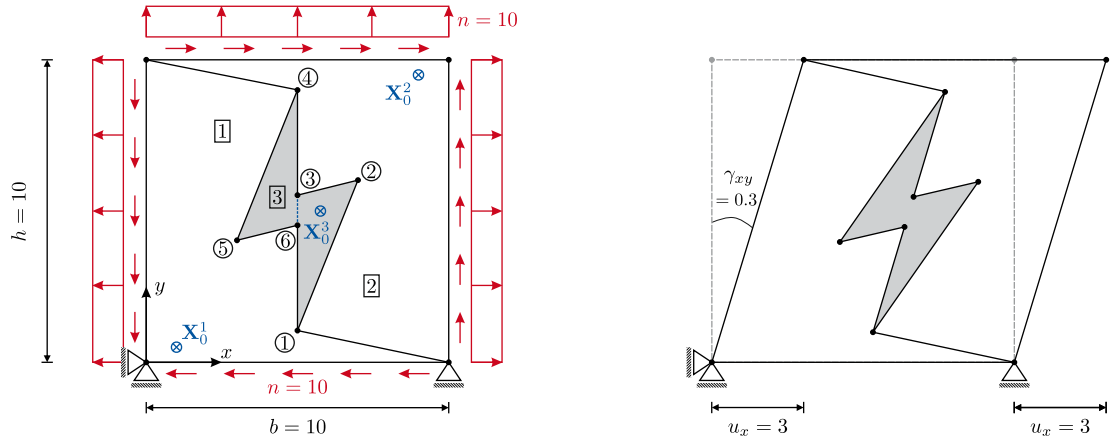

Figure 4: Non-star-convex patch test. (a) - Discretization, dimensions and loading. A possible set of scaling centers corresponding to elements 1, 2 and 3 are indicated. (b) - Deformed configuration and engineering shear strain γ_{xy}.

5.3 Perforated square plate

The performance of the proposed mixed scaled-boundary formulation can be compared to its displacement-based variant [7]. To do so, a perforated square plate of dimensions $b = h = 5$ and a

hole radius of $r = 1$ is investigated. The plate is subjected to a uniform tensile load $p = 20$ in the vertical direction. The material parameters are set to $E = 100$ and $\nu = 0.49$. We take advantage of the symmetry of the problem and analyze the upper right quarter of the plate. Symmetry boundary conditions are therefore employed at the left and bottom edges. Both quadrilateral and Voronoi discretizations (see Fig. 5) of the domain are taken into consideration.
Fig. 6a illustrates the convergence of the vertical displacement u_y^P of point P towards a reference solution, which is determined on an unstructured mesh consisting of nonlinear quadrilateral elements of sixth order [17] and 946,452 degrees-of-freedom. The corresponding relative error of u_y^P is shown in Fig. 6b. It is observed that for quadrilateral meshes, both scaled-boundary approaches yield the same solution. This is caused by the fact that by the scaling center was placed at the intersection point of the main diagonals, which excludes locking in the displacement-based element (see Section 5.1). As soon as the element geometry consists of more than 4 vertices, volumetric locking becomes inevitable in the displacement-based method and a locking-free scaling center position cannot be found. This is shown in Fig. 6, where the yellow solid line (r1d1) converges evidently slower than the blue solid line (B(1,0)S(1,0)) on the exact same Voronoi discretization. Still, one can recognize that the error corresponding to the Voronoi mesh is not perfectly linear. This discrepancy between the Voronoi and quadrilateral mesh is probably caused by the fact that the Voronoi mesh is not refined by the subdivision of a coarse mesh and all refinement steps are thus independent of each other.

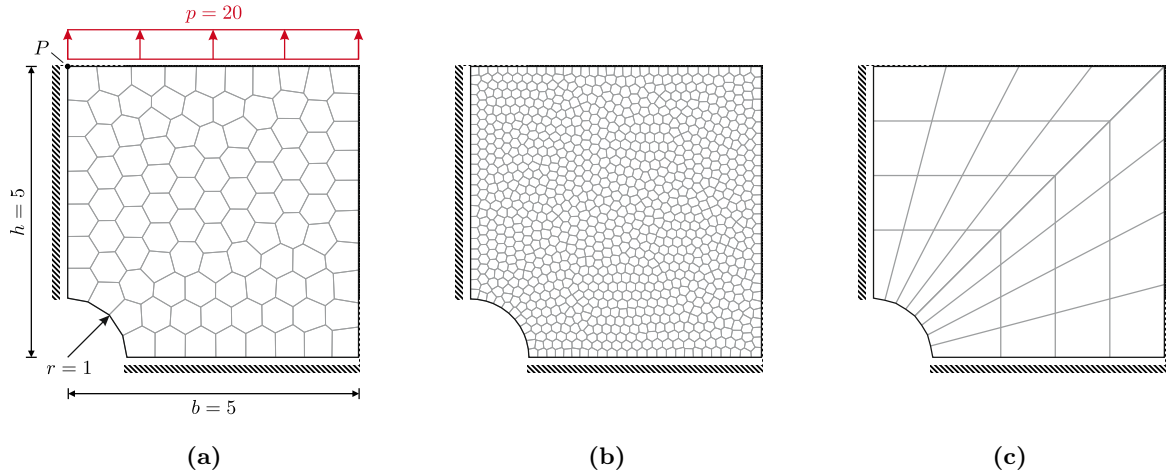

Figure 5: Perforated square plate. (a) - Discretization by 100 Voronoi elements, dimensions and loading. (b) - Global refinement towards 1000 Voronoi elements. (c) - Discretization by 32 quadrilateral elements.

Overall, it is shown that in this particular example, the proposed element behaves better on a Voronoi mesh than on a structured quadrilateral mesh. This accentuates a benefit of polygonal discretization methods in comparison to classical quadrilateral discretizations. Moreover, polygonal meshing-software can be applied to any geometry without partitioning the domain *a priori* and can be locally refined at low computational cost [18].

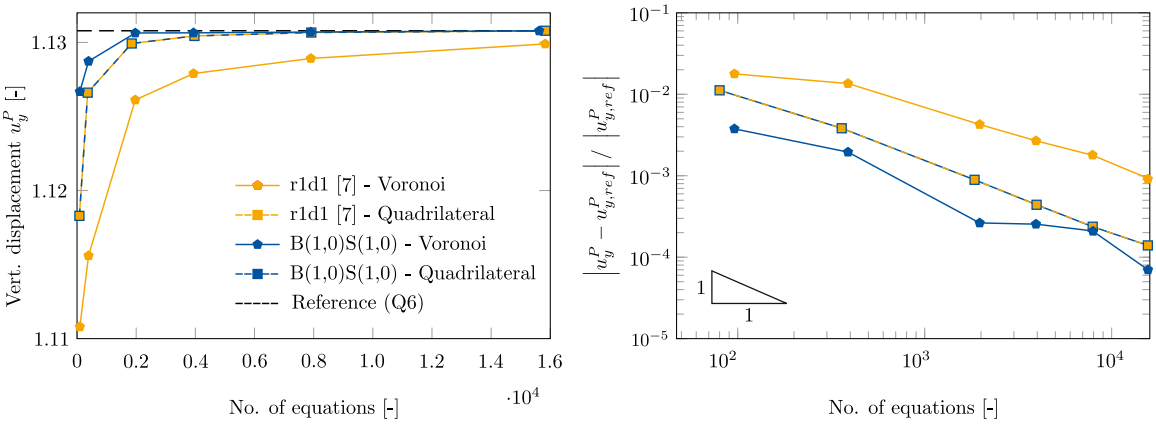

(a) **(b)**

Figure 6: Perforated square plate. (a) - Convergence of u_y^P for the r1d1 [7] and B(1,0)S(1,0) elements on Voronoi and quadrilateral meshes. (b) - Relative error of u_y^P with respect to the reference solution.

6 CONCLUSIONS

In this work, the occurrence of volumetric locking in displacement-based scaled-boundary finite elements with a numerically approximated scaling direction is handled by a mixed displacement-pressure formulation. In addition to this, pressure continuity must be enforced over sectional boundaries to fulfill the incompressibility constraint weakly in the polygonal domain. This allows the sectional domains to exhibit compressible deformations, whereas the superior polygonal domain remains (nearly-)incompressible.

The alleviation of volumetric locking is demonstrated by three examples. It was shown that in contrast to the displacement-based scaled-boundary formulation [7], the eigenvalues of the stiffness matrix remain uncoupled for the proposed method. Furthermore, it was shown that volumetric locking is fully excluded and its severeness does not correspond to the position of the scaling center. The nonlinear analysis of a perforated plate problem consisting of a nearly-incompressible Neo-Hookean material showed that the approximation error for the proposed method is up to 16 times smaller than its displacement-based counterpart. It was additionally shown that polygonal element discretizations are beneficial in comparison to quadrilateral element geometries and converge faster. This result presents a solid motivation for the use of polygonal finite elements, such as the proposed element formulation.

REFERENCES

[1] S. Natarajan, E. T. Ooi, C. Birk, and C. Song, "Adaptive modelling of dynamic brittle fracture-a combined phase field regularized cohesive zone model and scaled boundary finite element approach," *International Journal of Fracture*, pp. 1–22, 2022.

[2] R. Reichel, S. Klarmann, and S. Klinkel, "A polyhedral element formulation based on the scaled boundary method for the analysis of nonlinear problems in solid mechanics," *PAMM*, vol. 20, no. 1, p. e202000177, 2021.

[3] S. Natarajan, E. T. Ooi, I. Chiong, and C. Song, "Convergence and accuracy of displacement based finite element formulations over arbitrary polygons: Laplace interpolants, strain smoothing and scaled boundary polygon formulation," *Finite Elements in Analysis and Design*, vol. 85, pp. 101–122, 2014.

[4] C. Song, *The Scaled Boundary Finite Element Method: Introduction to Theory and Implementation*. Wiley, 2018.

[5] R. Behnke, M. Mundil, C. Birk, and M. Kaliske, "A physically and geometrically nonlinear scaled-boundary-based finite element formulation for fracture in elastomers," *International Journal for Numerical Methods in Engineering*, vol. 99, no. 13, pp. 966–999, 2014.

[6] Z. Lin and S. Liao, "The scaled boundary fem for nonlinear problems," *Communications in Nonlinear Science and Numerical Simulation*, vol. 16, no. 1, pp. 63–75, 2011.

[7] S. Klinkel and R. Reichel, "A finite element formulation in boundary representation for the analysis of nonlinear problems in solid mechanics," *Computer Methods in Applied Mechanics and Engineering*, vol. 347, pp. 295–315, 2019.

[8] M. Chasapi, L. Mester, B. Simeon, and S. Klinkel, "Isogeometric analysis of 3d solids in boundary representation for problems in nonlinear solid mechanics and structural dynamics," *International Journal for Numerical Methods in Engineering*, 2021.

[9] B. Sauren, S. Klarmann, and S. Klinkel, "A mixed acoustic fluid finite element in boundary representation for fluid-structure interaction," *PAMM*, vol. 21, no. 1, p. e202100158, 2021.

[10] U. Brink and E. Stein, "On some mixed finite element methods for incompressible and nearly incompressible finite elasticity," *Computational Mechanics*, vol. 19, no. 1, pp. 105–119, 1996.

[11] S. Hartmann and P. Neff, "Polyconvexity of generalized polynomial-type hyperelastic strain energy functions for near-incompressibility," *International journal of solids and structures*, vol. 40, no. 11, pp. 2767–2791, 2003.

[12] F. Brezzi and M. Fortin, *Mixed and hybrid finite element methods*, vol. 15. Springer Science & Business Media, 2012.

[13] B. Fraeijs de Veubeke, "Displacement and equilibrium models in the finite element method," *Stress analysis*, pp. chapter–9, 1965.

[14] K.-J. Bathe, *Finite element procedures*. Klaus-Jurgen Bathe, 2006.

[15] J. C. Nagtegaal, D. M. Parks, and J. Rice, "On numerically accurate finite element solutions in the fully plastic range," *Computer methods in applied mechanics and engineering*, vol. 4, no. 2, pp. 153–177, 1974.

[16] E. B. Chin and N. Sukumar, "Scaled boundary cubature scheme for numerical integration over planar regions with affine and curved boundaries," *Computer Methods in Applied Mechanics and Engineering*, vol. 380, p. 113796, 2021.

[17] P. Wriggers, *Nonlinear finite element methods*. Springer Science & Business Media, 2008.

[18] J. Zhang, S. Natarajan, E. T. Ooi, and C. Song, "Adaptive analysis using scaled boundary finite element method in 3d," *Computer Methods in Applied Mechanics and Engineering*, vol. 372, p. 113374, 2020.